HiSST: 4th International Conference on
High-Speed Vehicle Science Technology
22 -26 September 2025, Tours, France

Experimental characterization of morphing structure for space applications under thermal and mechanical load

S. Paris[1], S. Holum[1], S.Debaissieux[2], M. Wouters[2],*
A. Francois[3], A. Parmentier[3], S. Meyers[4],
W. Declercq[4], J. Steelant[5]

Abstract

Design of aerospace vehicles remains a real challenge and considerable room is left for improvement. Their aero-mechanical architecture becomes very complex when considering the Thermal Protection System (TPS) along with its appropriate sizing, characteristics related to their assembly with hot structures and specific parts like noses, leading edges and control surfaces. Aerospace missions demand for hypersonic systems able to withstand not only the very severe environment but also to perform some manoeuvres and to adapt the controllability of the vehicle and its propulsion unit. This requires the presence of moving parts operating in a hot environment with suitable sealing to avoid sneak flows or alleviating any weak point due to surface discontinuities in the aggressive high enthalpy reacting environment.

Hypersonic morphing offers the advantage to integrate the functionality of the high-speed system in a continuous shape eliminating the presence of gaps or leaky passages. It avoids having weak points in the structure that could potentially be fatal for the aerospace vehicle and would favour improved performances.

To investigate this morphing capability, as a conceptual solution for hypersonic system, a demonstrator based upon a high-temperature resistant materials was proposed having the capability to modify its geometry during operation in a high enthalpy flow.

The technical challenges were first to identify the specific applications for hypersonic systems most suitable for morphing capabilities, secondly, to elaborate a mechanical design of such a structure in parallel with the material development and manufacturing. As silicon carbide ceramics are well known for their high temperature resistance and chemical stability, make them ideal candidate materials for morphing structures. However, SiC ceramics are also stiff and do not deform easily. Therefore, dedicated geometrical architectures must be developed in order to ensure that the ceramic material can be used for morphing structures. These geometrical architectures cannot be fabricated with traditional ceramic manufacturing techniques, like die pressing or injection moulding. Additive manufacturing (AM) techniques, on the other hand, do have the potential to create these complex geometries. As this exploration is carried out by numerical tools, the material and manufacturing constraints were investigated together with the practical solutions that could be obtained. A strong interaction is therefore needed with the material developer to adjust at best the functionalities of the structure and the properties of the material. The final part is dedicated to the testing and validation of the developed structure considering its aerodynamics, thermal and mechanical behaviour. A sample is tested in "hot conditions" in a reacting plasma flow to test the material resistance and the aerothermal properties of the structure. A dedicated bench is developed for tests in the VKI-Plasmatron. It allows

[1] *Von Karman Institute for fluid dynamic. Chausee de waterloo, 72. 1640 Rhode Saint Genese. Belgium*
[2] *SONACA. RN 5 1/Z, 6041 Charleroi. Belgium*
[3] *CENAERO. Rue des Frères Wright 29, 6041 Charleroi*
[4] *KU Leuven. Celestijnenlaan 300, Box 2420, Office 01.190, 3001 Leuven, Belgium*
[5] *ESA ESTEC. Keplerlaan 1, 2201 AZ Noordwijk, The Netherlands*

 Copyright © 2025 by author(s)

to apply representative surface temperature (around 1000^{0}C) on a model. An actuator can deform the model gradually whereas the deformation and the stress can be measured during the tests. Results of these experiments are then compared with numerical model for validation.

Keywords: *Supersonic plasma, Material, Ceramic, Morphing.*

Introduction

The idea of morphing structures in aeronautics is nothing new and has been used actively from the start of flight, and is today used in most, if not all, aircraft. However, the use of morphing structures in aerospace is rarer due to the much harsher environment, especially the thermal environment. A morphing structure made of rigid materials which can survive the high heat fluxes, and corresponding temperatures, necessitates smartly designed hinges and gaps, with corresponding seals. Alternatively, one could envision a continuous flexible material for the same morphing structure, avoiding the need of seals, and the corresponding high temperature leak flow impacting the seal. Such a continuous flexible surface is no new concept and was used by the Wright Brothers already in their airplanes to achieve roll control [1]. However, it is only recently, with the advancement in material science and additive manufacturing, that flexible structures are a feasible solution for high-temperature applications.

1. Specific applications

1.1. Control surface

All aircraft need morphable control surfaces to control and steer the flight. For regular subsonic and to a lesser degree supersonic airplanes do not have particular problems with leakage flows and gaps, as long as it does not penetrate the cabin. For wings, rudders and unpressurised parts, there is no problem with airflow penetrating the skin into the underlying structure (within reasonable limits of course). However, for hypersonic vehicle, a freestream flow penetrating within the airframe is extremely hot. As the classical strategy of heat protection relies on a rigid, immovable heat shield, the presence of any movable surface demands particular attention. If control surfaces are designed as singular rigid structures, a gap between the vehicle body and the control surface is deemed necessary. This implies that hot sneak flow will leak through the gap due to the pressure difference across the control surface and come in contact with the unprotected structure beneath [2]. The best example of encountering this problem is the Space Shuttle. As the high heat TPS on the underside was rigid, complicated seals were needed to reduce the leak flow to acceptable levels. Two examples of high-temperature vehicles control surfaces are explored here, the ESA built Intermediate eXperimental Vehicle (IXV)and the NASA built Space Shuttle Orbiter (SSO). The Figure 1 gives the evolution of the temperature during the trajectory of the IXV. It shows that the surface temperature can reach 1000°C [3,4].

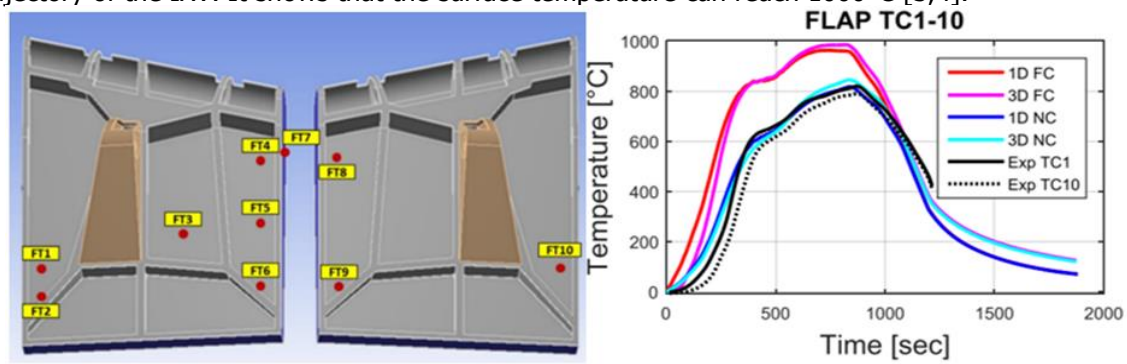

Figure 1 : IXV body flaps thermocouple positions (left) and related temperature measurements (right) [4]

Copyright © 2025 by author(s)

1.2. Scramjet and Ramjet

During the last twenty years, a large effort has been undertaken to improve knowledge on hypersonic air breathing propulsion, to acquire a first know-how for components design and to develop needed technologies. On this scientific and technology basis, two families of possible application can be imagined for high-speed air breathing propulsion: reusable space launcher and high-speed cruise vehicles. By combining the high-speed air breathing propulsion with a conventional turbo and/or rocket engine (combined cycle or combined propulsion system the average installed specific impulse along the ascent trajectory is increased resulting into more performing vehicles and, hopefully, a fully reusable one. A lot of system studies have been performed on that subject within the framework of different and consecutive programs relying on variable geometries [5,6,7,8] .
From the point of view of materials, the major technological difficulty for the development of hypersonic air breathing vehicles, powered by dual-mode ramjet or scramjet, is to design and realize the structure of the combustion chamber. As a matter of fact, the combustion chamber and the fuel injection and/or flame stabilization systems, possibly placed in the flow, must be able to sustain a rarely so severe thermomechanical environment.
Moreover, in the case of variable geometry combustion chamber, it is necessary to ensure a sufficiently controlled geometry to ensure tightness between movable and fixed surfaces of the chamber.
These elements lead to consider combustion chamber technologies based on the use of thermo-structural composite materials cooled by the fuel. By comparison with metallic solutions, such a technology should give large design margin and should correspond with relatively low-cost systems while ensuring good reliability and safety characteristics.

1.3. TPS

The thermal protection system (TPS) is the most crucial system for any spacecraft aiming to enter an atmosphere and survive. Currently, these are rigid structures which limit their size, and hence also the payload it can protect. The choice of material is dependent on the mission and the surface heat flux, directly caused by velocity of the vehicle. The range of heat fluxes for earth reentry ranges from 100 to 10 000 kW/m^2 [9] depending on the orbit and corresponding entry trajectory and position on aircraft [10, 11]. This range of 2 orders of magnitude imposes a great variation on the material, and no material is suitable across the whole range. For the fastest spacecraft with the highest heat flux, only ablative materials are a feasible choice. For slightly lower temperatures a reusable heat shield, usually made of ceramics, is feasible, famously employed on the Space Shuttle, which stretched the capability of such reusable materials. Much of data of TPS materials are cooperation secrets, but a review paper on TPS gives some material data on reusable (Space Shuttle) and ablative TPS material [12].

The material of a thermal protection system must fulfill multiple criteria. Three particularly critical ones are:

1. Survive the instantaneous peak surface heat flux.
2. Absorb the total entry heat load without exceeding the material temperature limit.
3. Survive the mechanical stress and without degrading simultaneously the aerodynamic performance.

The instantaneous surface heat flux and mechanical stresses will determine the maximum surface temperature and hence also the material type. However, the heat flux is the main driver of the material choice rather than the comparably low mechanical shear stress, but it cannot be neglected. The total heat load can also affect the material choice, but mostly relates to the sizing of the system itself and is not so crucial for the present purpose. These three criteria are assessed with respect to former reentering spacecrafts.

2. Requirements

The degree to what a material needs to be resistant with respect to heat fluxes and temperatures is largely dependent on the application. Apart from the high heat fluxes, the material also has to withstand the surface pressure and mechanical shear induced by the flow. Their relative importance varies wildly:

 Copyright © 2025 by author(s)

TPS materials mostly operate at peak heat fluxes in combination with quite low static surface pressures, whereas a scramjet operates at much higher pressure, and hence more severe mechanical shear and surface pressure conditions. In either case, large thermal gradients are present to keep internal parts cool. To keep thermal stresses low, the materials preferably have low thermal expansion rates and a high resistance to thermal shocks.

On top of that, since the materials for morphing structure have to be flexible, additional requirements need to be formulated. These include bend radius, trade-off between strength and flexibility, plastic vs elastic deformation etc. However, the implication that an increase in flexibility often goes along with a decrease in the material strength, makes the trade-off not trivial. E.g. in SiC additive manufacturing, an increase in silicon content provides a more flexible material but the heat resistance decreases as the amount of SiC is reduced. This trade-off requires good information on the bend radius and thermal environment needed for the application. Most of these values can be found in the Table 1 (mechanical shear has not been given as authors could not find sufficient information).

Application	**Heat flux [kW/m^2]**	**Surface temperature [K]**	**Surface pressure [Pa]**	**Bend radii [m]**	**Sources**
TPS Space shuttle (HRSI, Li-2200)	800	1500	35000-40000	Infinite	[9], [13], [14], [15]
Flexible TPS (SiC, Nicalon)	940	2073 (max)		~0 (2 inches) (packed)	[16]
Space Shuttle elevon (peak)	400 (800 when large deflection)	1500	5000		[9], [17]
Space Shuttle elevon cove gap	150-250 (800 when large deflection)	>1150	5000	1.5	[17], [9], [18]
IXV control surfaces	250	1400	3800	1.0	[3], [4]
IXV surfaces	450	1400	14000	Infinite	[3], [4], [19]
Scramjet conbustor		1800(cooled)	30000	8	[5], [7]

Table 1 : Main requirement for space applications

3. Scalability

Table 1 gives the main requirements for material according to the application. Whatever the case, the pressure remains below 5000Pa but the temperature and the heat flux can reach very high values. For scramjet applications, the AM technique offers the possibility to have porous material. It is not planned to test this kind of material in this project, but a porous, flexible ceramic can be a very good candidate for air intake as it needs to be cooled down. This can be part of future activities.
For control surface, the maximum temperature is found around 1400K for a heat flux of 250kW/m^2. The surface pressure of 5000Pa seems to be representative of the more critical flight conditions. The radius was estimated for the IXV vehicle. The value of 1m is considered as representative of a possible bending radius.

Requirements	Values
Max temperature	1400 K
Max heat flux	250 kW/m^2
Pressure	5000 Pa
Curvature radius	1 m

Table 2: Final requirement for the project (base on literature about control surface of reentry vehicle)

Copyright © 2025 by author(s)

4. Material development

Different material concepts were considered for the application selected in the MIMOSA[6] project. In order to comply with the thermal requirements, a ceramic material, i.e. reaction bonded silicon carbide (RBSC), was selected as the base from which these concepts would be developed. Furthermore, additive manufacturing (AM) via laser powder bed fusion (LPBF) was selected as a production method, since it allows for unlimited design freedom, fast prototyping and economical production of unique pieces or small production volumes. The material concept development, initial testing and selection is detailed in [20]. In the following paragraphs, the final selected material and its production methodology is detailed, along with the manufacturing of the hot demonstrator components for the Plasmatron testing.

The final material selected for the demonstrator fabrication was a reaction bonded silicon carbide: a ceramic composite material consisting of SiC, residual Si and residual C. RBSC is produced via a powder metallurgy process, in which a feedstock powder is shaped into a porous preform with the desired geometry. This porous is then infiltrated with C and subsequently with Si in order to close the residual porosity. In addition, a reaction takes place between the C and the Si resulting in a reaction formed SiC.

The required porous preform can be fabricated via conventional shaping methods, like uniaxial pressing or ceramic injection moulding. However, in this work, LPBF 3D printing was used to shape the powder feedstock into the desired geometry. This results in a porous preform which then needs to be densified by a number of post-processing steps. The entire process methodology, containing 6 steps, can be seen in Figure 2.

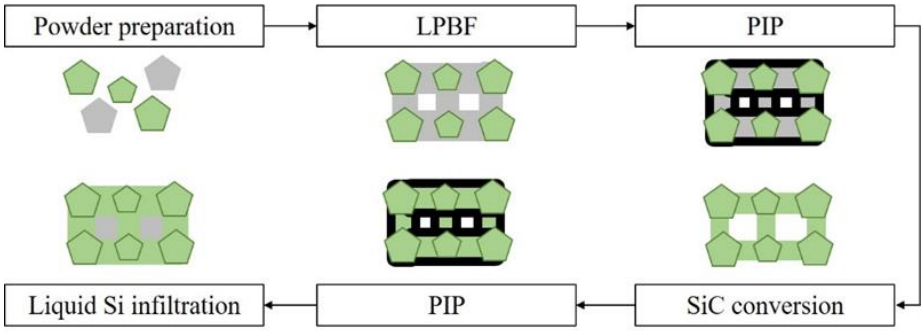

Figure 2: Six-step powder metallurgy process for the production of reaction bonded silicon carbide via LPBF 3D printing, for the manufacturing of hot demonstrator components for further plasmatron testing at VKI

The six steps are detailed as follows:

1. Powder preparation: a mix of Si (Nanoval, d_{50} = 26.2 µm) and SiC (Washington Mills, d_{50} = 29.2 µm) powders was prepared by adding them in a 40:60 volume ratio to a poly-ethylene container and mixing them for 5h at 75 rpm in a multi-directional Turbula mixing/milling device.
2. LPBF 3D printing: the prepared powder mix is used in a typical metal LPBF machine, i.e. a ProX 320 (3D Systems), equipped with a 500 W continuous wave fiber laser with a spot size ($1/e^2$) of 90 µm and a wavelength of 1070 nm. Thin layers of powder are spread out onto a build plate and subsequently selectively scanned by a laser. The Si in the powder mix melts and re-solidifies, binding the SiC particles in a "slice" of the desired component. This process is repeated layer-by-layer until the desired 3D geometry is obtained. LPBF was done with a laser power P of 50 W, a scanning speed v of 800 mm/s, a layer thickness l of 30 µm and a hatch spacing h of 100 µm. The scanning was performed in a continuous, zig-zag pattern with a 67° rotation between layers for process optimization, and the process was conducted under an

[6] MIMOSA: Morphing of aero-thermally loaded structures. ESA GSTP Contract No. 4000140022/22/NL/MG

Copyright © 2025 by author(s)

inert Ar atmosphere (< 25 ppm PPM O_2). LPBF resulted in porous preforms with a relative density of about 55%.

3. PIP: the porous preforms produced via LPBF were subsequently infiltrated with carbon via polymer infiltration and pyrolysis (PIP). To this end, an in-house produced phenolic resin was infiltrated at room temperature via vacuum infiltration. The infiltrated components were then heat treated in a tube furnace to cross-link (3 hours at 150°C) and pyrolyse (2 hours at 700°C) the resin, yielding porous carbon into the preforms. The thermal cycle was executed under an inert nitrogen gas atmosphere. A total of 2 PIP cycles was performed to load the 3D printed preforms with carbon, resulting in porous components containing SiC, Si and C.
4. SiC conversion: the porous components from step 3 are treated in a graphite vacuum furnace (W100/150-2200-50 LAX, FCT Systeme) at 1500°C for 30 minutes with the aim of converting the present Si into SiC via the reaction with C (Si (l) + C (s) --> SiC (s)). This was done at a vacuum level of 40 mbar. The result of this step is a porous component consisting of SiC and C, where the present Si has fully converted into SiC.
5. PIP: similar to step 3, two extra PIP cycles are performed in order to further load the porous preforms with extra carbon. These PIP cycles were performed in exactly the same fashion as those presented in step 3.
6. Liquid Silicon Infiltration (LSI): finally, the SiC-C porous preforms were infiltrated with liquid silicon. This was done in the same graphite vacuum furnace as described in step 4, at a temperature of 1500°C for 30 minutes. The porous preforms were placed in a graphite crucible lined with BN, and Si chunks were placed underneath the component. At temperatures in excess of 1410°C, the Si melted and infiltrated the porosity due to capillary action, reacting with the present C to form more SiC. The end result was a RBSC component consisting of 62 vol% SiC, 28 vol% Si and 10 vol% C.

The relevant properties of the produced material are listed in Table 3

σ_{flex} [MPa]	ε [%]	E [GPa]	k [W/mK]	ρ [g/cm³]
221 ± 21	0.10 ± 0.011	266 ± 5	136	2.8

Table 3: Mechanical & thermal properties of the optimised RBSC.

In order to test the material's suitability for morphing control surfaces, two different "hot demonstrator" components were designed, a "blade" hot demonstrator and a "pillar" hot demonstrator. Both designs were manufactured according to the powder metallurgy process detailed in the previous paragraphs. However, since previous experiments were performed on 10x10x10 mm³ cubes to obtain optimised process conditions, the increased size and complexity of the hot demonstrator components posed additional challenges, especially for LPBF. Various scanning strategies were attempted, before settling on an island scanning strategy to replace the continuous zig-zag scanning. During island scanning, the cross-section of the component to be scanned is subdivided into 10 x 10 mm² islands, corresponding to the size of the cubes used to optimise the process in previous experiments. These islands are scanned in order. A dedicated scanning strategy was also developed for the pillars, since they represent very small (diameter 0.9 mm) cross sections. A multi-contour scan strategy was employed, where concentric contours were scanned in quick succession.

During production, in-process warping was observed, despite the significant efforts carried out to develop dedicated scanning strategies. Due to the large cross-sections of the demonstrator components, very large heat inputs are delivered to each layer. Upon cooling, as the layer shrinks, it is initially constricted by its attachment to the base plate and/or the previously scanned layer. Eventually, the corners of the component come loose and bend upwards due to the thermal stresses. All in all, in-process warping resulted in a failure rate of approximately 50%. Nevertheless, 3 successful blade and 4 successful pillar concepts were produced via LPBF and subsequent post-processing, one of which is shown in Figure 3.

Copyright © 2025 by author(s)

Figure 3: **Finished pillar stiffener Si-SiC hot demonstrator component.**

The resulting components were measured, and their dimensions were compared to the design (CAD-model) to assess the dimensional accuracy of the production route and as extra information and input for the test campaign. The measurements showed that there was a small discrepancy between the as-fabricated and as-designed components. Plate and blade thickness values were consistently 200 µm larger in the real components when compared to the design. Hole diameters were very similar, although slightly smaller in the real component (up to 150 µm). Pillar diameters were consistently 100 µm larger than designed. All of these deviations are a result of the post-processing infiltrations, which have the potential to cause slight oversizing (and therefore hole diameter undersizing) due to excessive / over-infiltration. The most important deviation with respect to the CAD design, however, is caused by the in-process warping. A flatness criterion of 0.15 mm was set forth; however, this was exceeded, and in some cases the difference between opposite ends of the component (bottom of the plate, as illustrated on Figure 4 as "curvature") was over 1 mm. Measurement points on the pillar hot demonstrator are the same, with the exception of having the fin thickness being replaced by the pillar diameter.

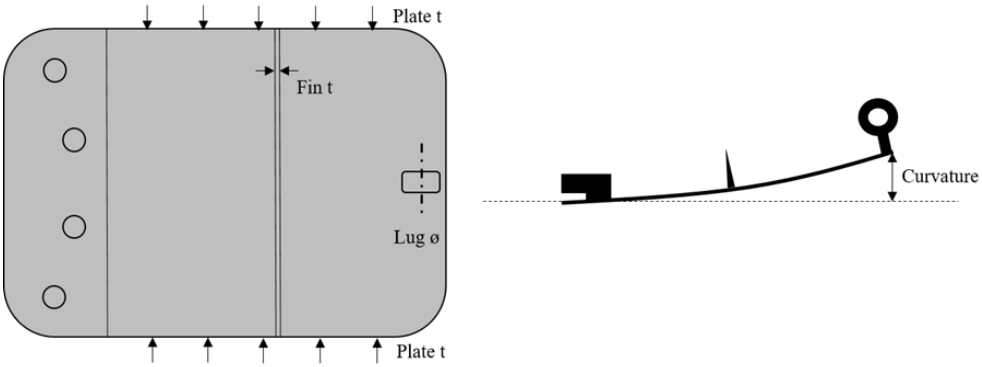

Figure 4: Schematic view of measurement points on the fin hot demonstrator.

5. Experiment under plasma conditions

5.1. The Plasmatron

The selected materials are tested in the high-enthalpy Plasmatron facility at the VKI in a high-temperature environment relevant to their application. The Plasmatron consists of an Inductively-Coupled Plasma generator of 1.2 MW attached to a vacuum chamber. Supersonic flows can be achieved with converging-diverging nozzles placed at the exit of the plasma torch. For this activity, we plan to use a nozzle with semi-elliptical exit cross section that provides a flat plate test bed, which has recently been commissioned at VKI under the ESA GSTP activity: ESA Space debris (Contract no.

Copyright © 2025 by author(s)

4000125437/18/NL/RA). In a test run, the plasma flow is discharged onto the flat plate mechanism, holding the material sample at the exit of the nozzle (Figure 5).

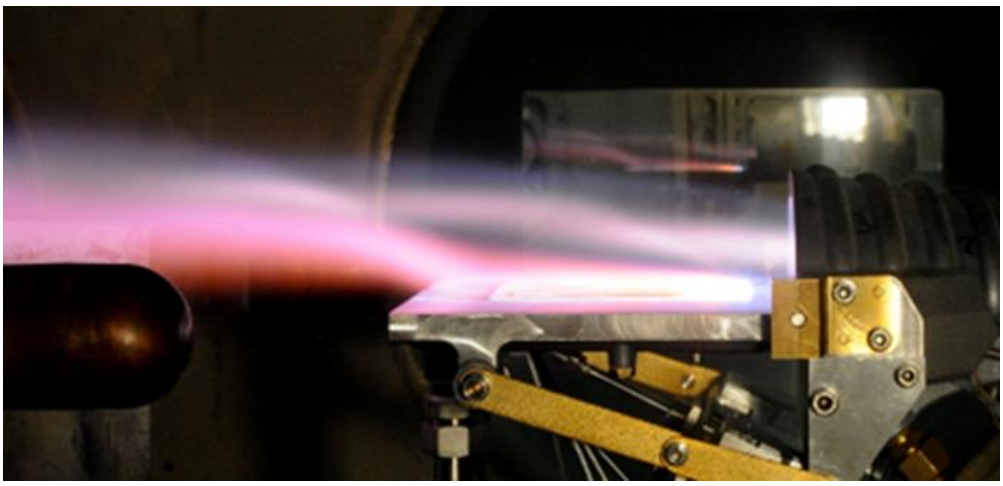

Figure 5 : Flat plate testing at the VKI Plasmatron.

In this task, the Plasmatron test set-up (Figure 5) was upgraded to interface the (hot) demonstrator and to protect the morphing structure and actuator(s) from the plasma flow.
The size of the test samples is about 80mm x 90mm. Air mass flow (and by this total reservoir pressure), vacuum chamber pressure and electric power applied to the coil are the main independent parameters driving a Plasmatron test under supersonic conditions. According to CFD, the Mach number at the exit of the nozzle vary from 2.8 to almost 4 in the jet.

5.2. Experimental set-up

The instrumentation used for actuating and measuring the resulting force from bending the plate needs to be encased in a cooled environment to survive inside the Plasmatron. A water-cooled cooper pipe spiral with a steel lid and encasing was constructed to keep the instrumentation safe. It can be seen mounted inside the Plasmatron in Figure 6 (left). In the Figure 6 (right), the cold box is removed to show the actuator. The balance will be inserted at the extremity of the motor.

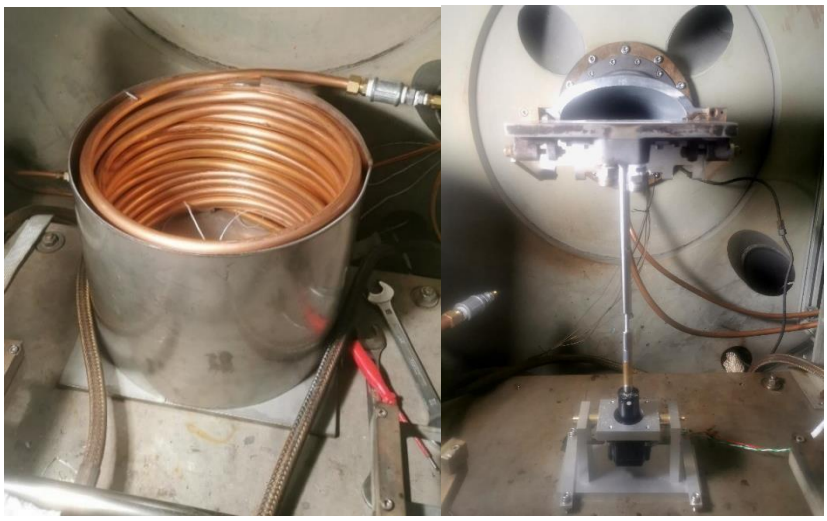

Figure 6: Cold box and actuator

Copyright © 2025 by author(s)

5.3. Instrumentation

The control parameters are mainly the mass flow of gas, the static pressure inside the test chamber, and the power applied to the coil. The chamber is fitted with portholes allowing optical access to the plasma jet. A comprehensive setup has been developed and applied to the facility for material response analysis. The Plasmatron is equipped with several intrusive and non-intrusive techniques. All instruments are calibrated before the test campaigns. Below a summary of the equipment used for these tests:

(a) Infrared camera (FLIR) [3-5.3µm, 500-3000°C],
(b) 2-colour pyrometers (Raytek) [0.75-1.1µm, 700-3000°C],
(c) Broad band radiometer (Heitronics) [0.6-39µm, 250-2500°C],
(d) 2 high-resolution cameras (Allied vision Prosilica GT2050 and GT2000)

To measure the deformation of the plate during test, a setup previously used to measure recession of material samples in the Plasmatron is used. The setup consists of a Prosilica GT2050 camera with a 190-430mm telescopic lens. The telescopic lens is used to increase the spatial accuracy of the camera setup. The camera has a resolution of 2048x2048 and 28fps. The regular setup gives around 0.1mm resolution, but this can be improved by zooming in with the lens. The setup is lined up using a suspended laser.

The actuator was selected for his ability to support high temperature. The cold box should be capable of maintaining the temperature of the motor below 70°C but as it is the first time we are using a step motor in the Plasmatron, we selected a motor capable to support 180°C. The other criteria were the force, the accuracy of the position and the stroke.
The selected motor is from Haydon, with reference 57H4A-12-A23. The stroke is 38.4 mm. A single step is 0.0079 mm which offers a very high positioning accuracy while the maximum force is about 1400N. During the test, there is no encoder to estimate the displacement, the number of steps sent to the motor is used to deduce the position. Because of the thermal expansion of the beam connecting the motor to the sample, it was preferred to adjust the position of the actuator to maintain the force constant and to limit the risk of breaking the plate.
The selected balance is a "Precision Miniature Tension and Compression Load Cell from Burster. The model 8431- 5100 is used for the hot test. It can support 120°C which is comfortable according to the first measurements made in the cold box. This balance can measure up to 100N.

5.4. Test conditions

Due to the relatively recent addition of the supersonic semi-elliptic nozzle into the Plasmatron [19], the flow environment is not fully categorized. Experimental campaigns are underway to measure surface pressure and surface heat flux distributions where material samples are installed. The preliminary results are done at varying the Plasmatron control parameters, i.e. air mass flow, electronic generator power, plate angle of attack and chamber pressure. The average heat flux over the plate is around 100kW/m^2 at 0° AoA and 400kW/m^2 at 10°AoA and surface pressure from -200Pa (pressure pulling the plate upwards) at 0° AoA and high chamber pressure while with 10°AoA the surface pressure is maximum 250Pa (pushing the plate downwards) at high mass flow (12g/s). This shows that the surface pressure requirement of 5000Pa from the literature survey is impossible to reach in the Plasmatron facility. However, the heat fluxes encompass the 250kW/m^2 set in the requirement. However, no condition measured correspond to this heat flux, and there are still high uncertainties in the heat flux measurements. Therefore, the surface temperature was set as the target requirement to meet. To ensure that the sample will survive and give useful deformation data the target surface temperature was set to 1000°C for Si-SiC plates. Similarly, to avoid surface oxidation on titanium and altering the material properties, the max surface temperature of the titanium samples were set to 500°C. To track the surface temperature of the Si-SiC test sample the Raytek Pyrometer was used. For the titanium, a Heitronics radiometer was used. Emissivity was hard to determine and the temperature here is uncertain. However, limited surface oxidation was observed. All tests were done at at 0°AoA, and the chamber pressure was increased to increase the surface temperature to the target for the Si-SiC test. The test conditions are then:

Copyright © 2025 by author(s)

Material	P_{el} [kW]	M_{gas} [g/s]	$P_{chamber}$ [mbar]	$P_{reservoir}$ [mbar]	Gas	$T_{surface}$ [K]
Si-SiC	501±3	8±0.01	4.91±0.88	175±2	Air	1223±40
Titanium	300±13	~5	2.42±0.11	121±5	Argon	797±12

Table 4: Plasmatron test conditions after initial transient when changing from argon to air. OBS: $T_{surface}$ for Titanium assumes an emissivity of 0.4.

5.5. Test articles

The models are inserted in a water-cooled aluminum support. A layer of alumina (insulating material supporting high thermal load) is placed between the cold support and the plate (see Figure **7**). Three different models have been developed:

1. Titanium thin flat plate without reinforcement.
2. Si-SiC model with a blade in the middle
3. Si-SiC model with a special support structure capable of distributing stress along the model as seen in the Figure **8**.

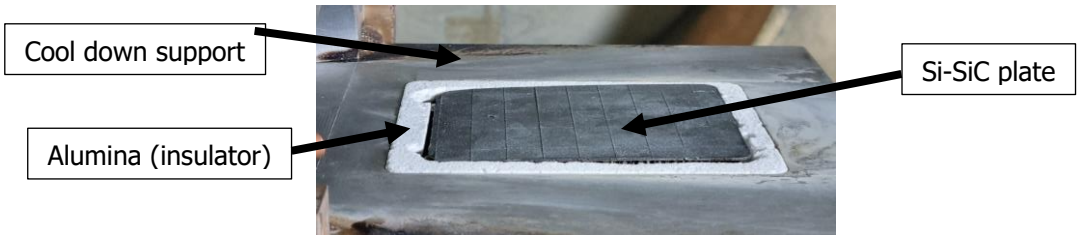

Figure 7 : Si-SiC models in the support

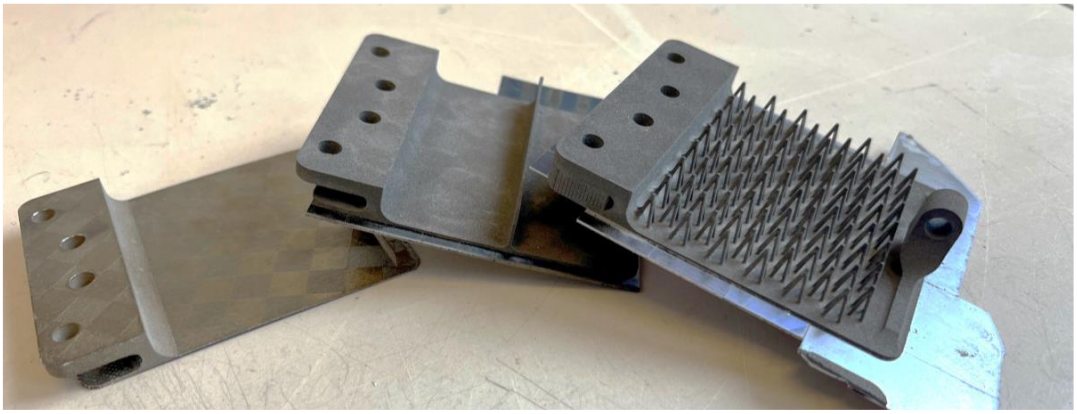

Figure 8 : Titanium and Si-SiC models as printed. From left to right: titanium, Si-Sic with blade and Si-SiC with support structure.

6. Thermo-mechanical modeling

A finite element model has been setup to analyse the thermomechanical response and evaluate the stresses in the samples as they are deformed by the actuator and heated by the plasma. The model is illustrated in Figure 9, featuring the Si-SiC blade sample and accounting for the symmetry of the design. Initially, a steady-state thermal model was established by assuming a uniform temperature of up to 1000°C on the surface exposed to the plasma. Heat losses, due to radiation and thermal conduction within the cooled supporting plate are taken into account. Additionally, contact conditions between the sample, the spacer and the cooled support are implemented to model the load and heat transfer. Fixation bolts are not directly modelled but are represented by a pre-loading force of 1000 N.

Copyright © 2025 by author(s)

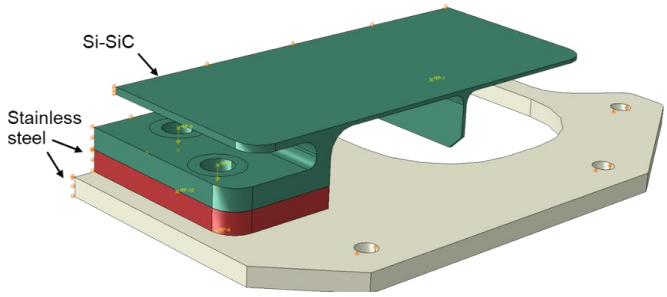

Figure 9: Thermomechanical model of the Si-SiC blade and its supporting structure

The material properties of Si-SIC used for numerical analysis are provided in Table 3. Mechanical and thermal properties of the Si-SiC at 1000°C were obtained by extrapolating values from lower temperatures. A Young's Modulus value of 243 MPa at 1000°C is used in the model.

Figure 10 illustrates the geometries of the two Si-SiC samples and the titanium sample, viewed from the side. The gray shapes represent the initial CAD geometries, while the green shapes depict the deformed geometries obtained from the numerical models when a vertical displacement is applied to the actuator.

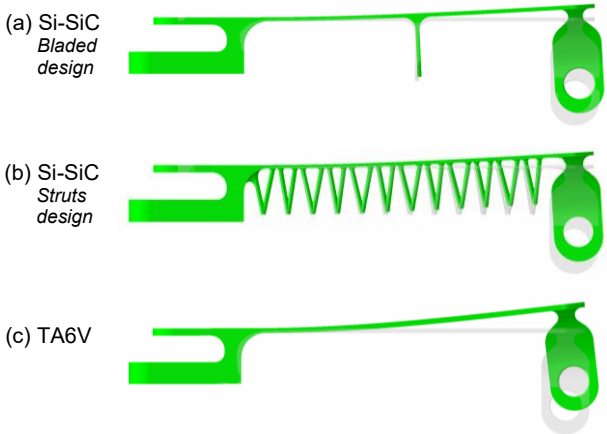

Figure 10 Geometries of titanium and Si-SiC samples when deformed (in green) and initial undeformed (in gray) for (a) Si-Sic with blade, (b) Si-SiC with structures and (c) titanium.

Figure shows the computed Von Mises stresses induced by an actuator displacement of +2.5 mm along with the thermal stresses resulting from heating the top surface at 1000°C for both Si-SiC samples. For the bladed design, maximum stresses of 213 MPa are observed, while higher stresses (up to 524 MPa) are computed for the Si-SiC sample with triangular structures, primarily due to local stress concentration at the junction of the structure's beams.

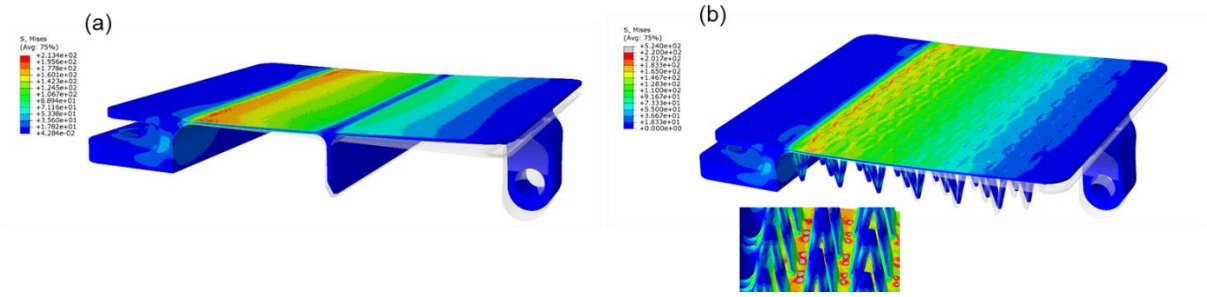

Figure 11 Stress induced by an actuator displacement of +2.5 mm for (a) Si-SiC blade and (b) Si-SiC with structure. Both samples are heated to 1000°C.

The mechanical properties of the titanium alloy differ significantly from those of Si-SiC. On one hand, the yield strength of the titanium alloy is considerably higher than that of SiSiC at room temperature, allowing for greater deformation and flexibility. However, its mechanical properties decrease much more rapidly with increasing temperature. For this reason, simulations were computed for intermediate

Copyright © 2025 by author(s)

temperatures and reflects the tests performed in the plasmatron at a lower power level. Figure 12 shows the stresses for the titanium sample induced by an actuator displacement of +5.0 mm along with the thermal stresses and evolution in material properties resulting from heating the top surface at 20, 600, 800 and 1000°C. The decrease in stress values with increasing temperature is directly related to the reduction in material stiffness and should be compared to the decreasing yield strength. At 1000°C, irreversible deformations are observed due to due to plastic deformations.

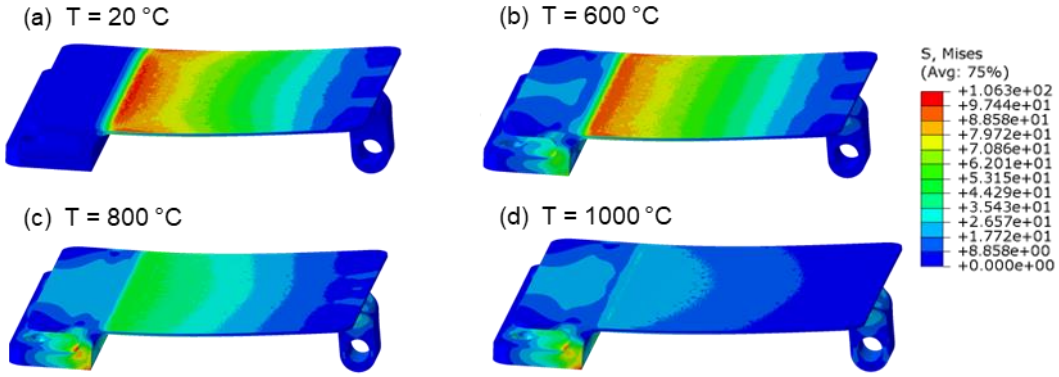

Figure 12: Stress induced in the titanium sample by an actuator displacement of +5 mm and surface temperature at (a) 20°C, (b) 600°C, (c) 800°C and (d) 1000°C.

The reaction forces measured at the actuator as a function of the imposed displacement are summarized in Table 5 for the different geometries. Based on these simulation results, the maximum allowable displacements can be determined before reaching failure of the Si-SiC sample or irreversible deformations of the titanium sample.

Si-SiC bladed - FEM results

	20 °C	1000 °C
Actuator displacement [mm]	2.50	2.50
VM stress (max) [Mpa]	224.70	213.40
Reaction force [N]	26.28	22.61

	20 °C	1000 °C
Material UTS [Mpa] [5]	200.00	*200.00*
Estimated actuator displacement at rupture[mm] [5]	*2.23*	*2.34*
Estimated reaction force at rupture [N] [6]	*23.39*	*21.19*

Si-SiC with structure

	20 °C	1000 °C
Actuator displacement [mm]	2.50	2.50
max VM stress located in struts [Mpa]	460.40	445.80
max VM stress located in plate [Mpa]	310.10	275.60
Reaction force [N]	21.29	22.61

	20 °C	1000 °C
Material UTS [Mpa] [5]	200.00	*200.00*
Estimated actuator displacement at rupture [mm]	*1.09*	*1.12*
Estimated actuator displacement at plate rupture [mm]	*1.61*	*1.81*
Estimated reaction force at rupture [N]	*9.25*	*10.14*
Estimated reaction force at plate rupture [N]	*13.73*	*16.41*

Titanium sample

	20 °C	600 °C	800 °C	1000 °C
Actuator displacement [mm]	5.00	5.00	5.00	5.00
VM stress (max) [Mpa]	229.70	131,4	60,9	33,6
Reaction force [N]	41.95	23.75	10.22	5.00

	20 °C	600 °C	800 °C	1000 °C
Material yield stress (Sy) [Mpa] [5]	*850.00*	*350.00*	*50.00*	*20.00*
Estimated actuator displacement at yield stress [mm] [5]	*18.50*	*13.32*	*4.11*	*2.98*
Estimated reaction force at yield stress [N] [6]	*155.22*	*63.26*	*8.39*	*2.97*

Table 5: Force and displacement on models made of titanium and Si-SiC (left are the computed values, right are the values estimated to reach rupture or yield stress)

Following the initial tests conducted in the plasmatron, a transient thermomechanical analysis was developed to evaluate the impact of the rapid application of the heat flux and the resulting thermal shock. In this transient model, the imposed temperature is replaced by a heat flux of 250 kW/m² applied on the surface exposed to the plasma. The thermal dissipation through radiation and conduction in the water-cooled support from the steady-state model were retained. These conditions lead to maximum temperature close to 1000°C, and a steady state temperature regime reached after 300 s.

Copyright © 2025 by author(s)

Figure 13 shows the time evolution of the maximum temperature and maximum stress computed in Si-SiC blade sample. The calculated stresses increase rapidly at the beginning of the heating phase, reaching a maximum significantly above the rupture limit of Si-SiC after approximately 17.6 seconds (illustrated Figure 14), before decreasing until a steady state regime is achieved. Stress concentrations are observed with significant temperature gradients that develops during the thermal transient, particularly in regions with variation in thickness. This analysis underscores the importance of considering the thermal transient regime simulations for the structural design phase, rather than relying solely on steady-state modelling conditions.

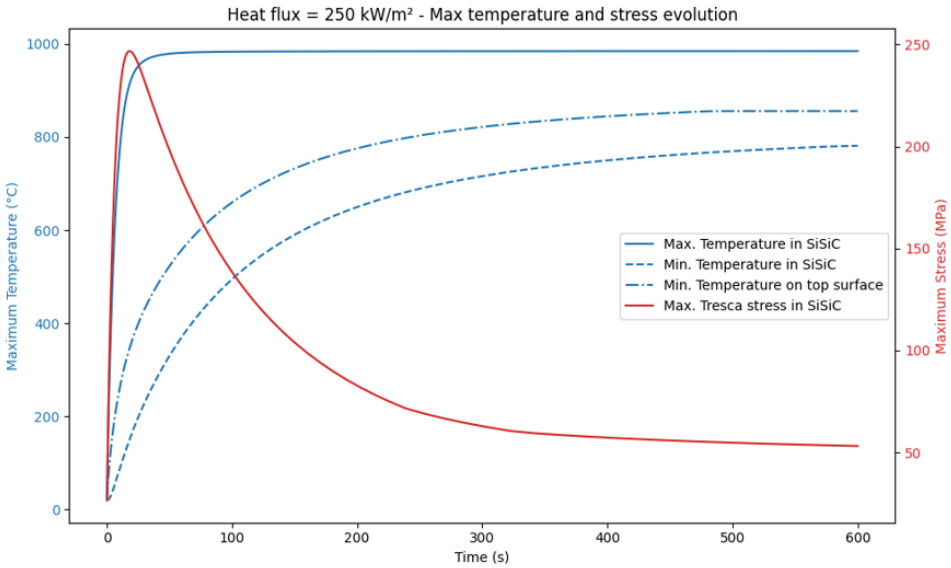

Figure 13: Evolution of the maximum temperature and maximum stress computed in Si-SiC blade sample with a heat flux of 250 kW/m²

(a) Temperature (*C) **(b) Stress [MP]**

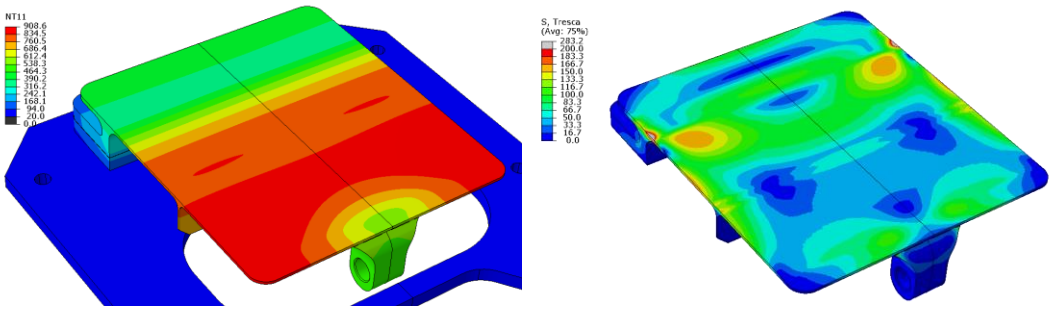

Figure 14: Temperature (a) and stress distributions (b) represented at t=17.62 s

7. Results and lessons learned

Tests were conducted first with the titanium plate. Titanium material can support high temperature but after some unsuccessful tests, it was decided to perform the test at lower temperatures (500°C) to avoid the oxidation and to maintain reasonable mechanical properties (above 500°C, there is a severe degradation of the properties). For the first test, during the transition from argon to air, the heat flux becomes very high, and the surface temperature exceed 1200°C. As the thermal expansion was very fast, the sample expanded up to and beyond the end of the cavity and started to bend.

Copyright © 2025 by author(s)

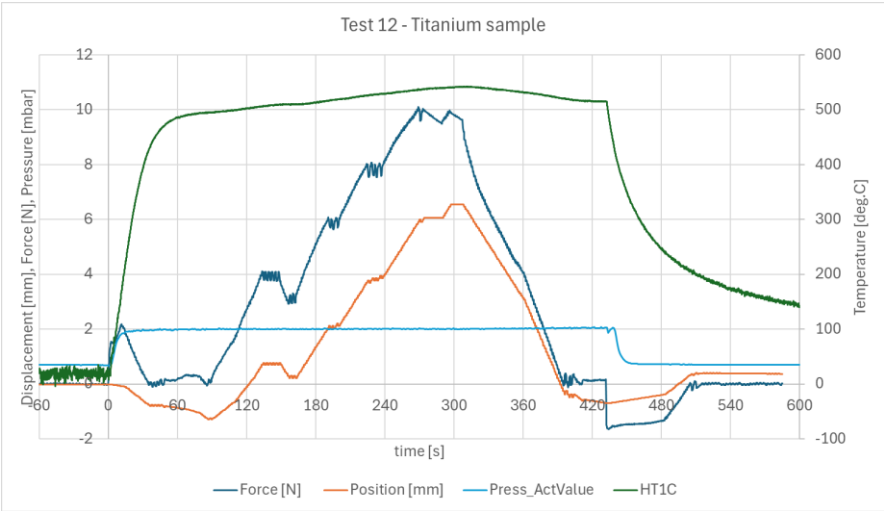

Figure 15: Results with titanium sample

Figure 15 gives the displacement and the force during the test. During the first 90 seconds, test conditions are adjusted. The actuator moves down (z=-1.2mm) to maintain the force at zero. Then, starting from this point, the force is increased by step (4N, 6N, 8N and 10 N). the corresponding displacement is shown on the orange curve. The deformation increases up to 7.5mm. The deformation observed from the side windows is in line with these measurements (slightly lower, about 6.5mm). According to the thermomechanical computation shown in Table 5, a displacement of 5mm is produced by almost 24N at 600°C. Measurement in the plasma wind tunnel gives experimentally only about 8 N. Figure 16 shows the plate before and after deformation (the plate was initially deformed during the manufacturing). The infra-red image extracted when the deformation is maximum shows a reasonable uniformity. There are two "cold regions" due to the local higher thickness.

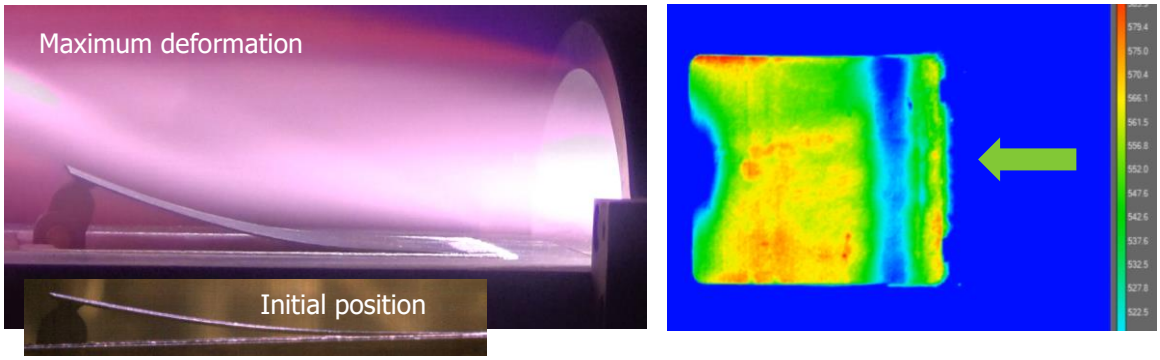

Figure 16: Titanium sample view from the side and from the top in IR. Initial position shown in bottom left corner

The thicknesses of the Si-SiC samples made with a blade and with triangular support structure were respectively 0.8mm and 0.7mm. Due to the material brittleness and low thickness, some samples were broken during the assembly into the sample holder. As the purpose is to reach 1000°C with this material, the tests were first conducted with argon, then a gradual transition towards air started up ending up with a complete switch-off of argon. Once the transition was complete, the pressure could then be adjusted. However, during this transition, the heat flux can jump suddenly, producing thermal stress and destroying the sample. Therefore, the transition must be as slow as possible. It was also noticed that the heat flux was very sensitive to the pressure. The pressure was limited to 5 mbar to avoid large heat flux gradient when the pressure exceed this limit. Another reason of the failure is the change in flow topology, i.e. shock structure, when the pressure is changing. Once a shock is impinging the surface, the resulting temperature gradient creates thermal stress which might break the sample.
Fortunately, more Si-Sic sample than initially planned were delivered.

Copyright © 2025 by author(s)

Figure 17 shows the results from the successful test performed with this material. The sample was equipped with the triangular support structure.

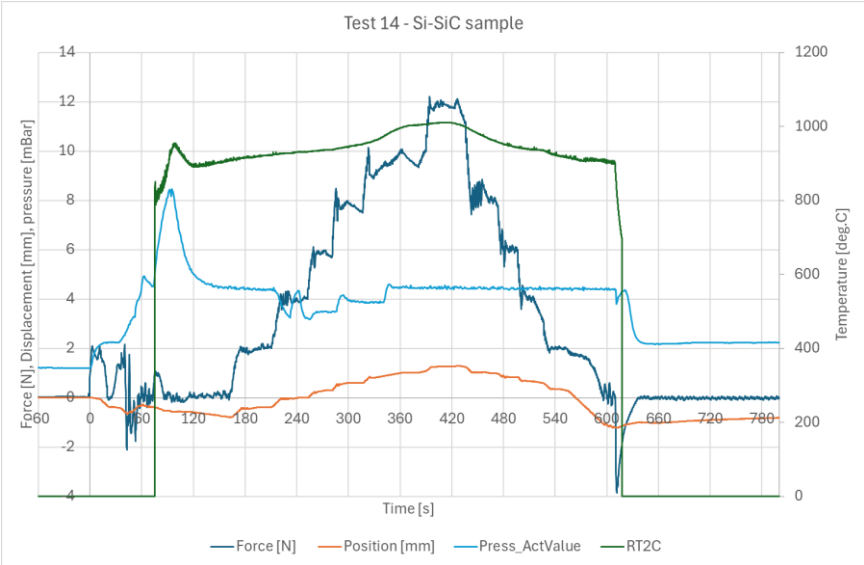

Figure 17: Results with Si-SiC sample

It takes about 150 second to start the Plasmatron, to pass from argon to air, and stabilize the temperature and the pressure. During this phase, the actuator is moved down to maintain the force at zero N. The beam connecting the motor to the plate is exposed to the plasma and expands. On the Figure 18, you notice a second beam connecting the water-cooled support. When it expands during the test, the support moves up and the actuator must correct its position to maintain a constant force. In order to minimize this effect, this beam was covered with DALFRATHERM®-1430 ZR BLANKET (a very good insulator). When conditions are stable, the force is stepwise increased (2N, 4N, 6N, 8N, 10N and 12 N). the corresponding displacement is shown on the orange curve. The deformation increases up to 2.1mm from -0.8mm to 1.3mm). The deformation observed from the side windows show a higher deflection of around 2.8mm.
According to the thermomechanical computation shown in Table 5, a displacement of 1.8mm is produced by 16.27N at 1000°C. Measurements in the plasma wind tunnel only give about 10 N for this displacement.
The reasons of this discrepancy are still under investigation. The thermo-mechanical properties at high temperature and the related non-uniform temperature distribution can be a part of this difference.

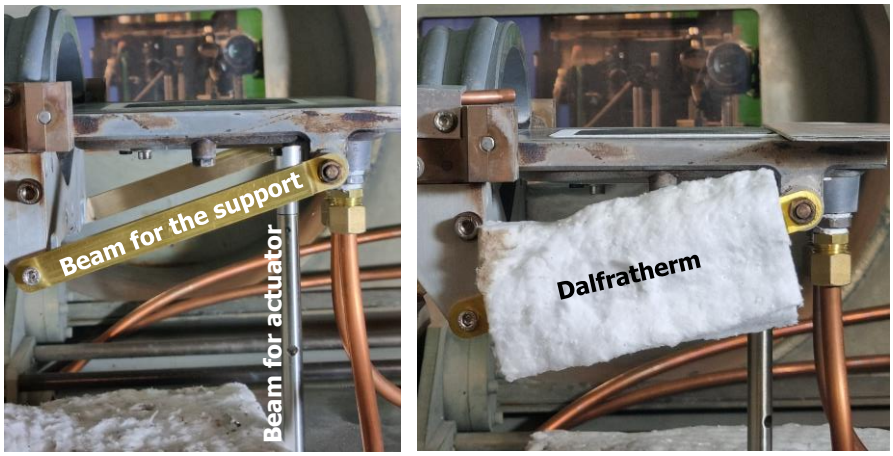

Figure 18: Thermal protection or the beam connecting the support

Copyright © 2025 by author(s)

The balance installed in the cold box should not be affected by the temperature effect as it remains much below the limit of the manufacturer. The balance measures the force due to the resistance of the material and the force due to the pressure on both sides. Considering 500 Pa as the pressure in the test section, this corresponds to 3.5N on the bottom face where there is no flow. The top surface is subject to supersonic flow. According to surface pressure measurements performed on a flat plate in similar condition, the pressure on the top surface is around 300-400Pa (depending on the location along the plate), producing 2.5 N. This means a correction should be applied on the force given by the balance. The actual force induced by the material is 1 N higher than the one given by the balance.

8. Outcome of the study

The purpose of this project was to deform material under high thermal load and to reach a radius of curvature of 1m. Two materials were investigated, the titanium and the Si-SiC.
The facility has been modified to perform these tests. A stepper motor and a balance were installed in a cold box, allowing to deform the material during the test under plasma. The measurement of the force and the displacement imposed by the motor is precise, but correction must be applied to consider the thermal expansion of different element, and the force induce by the pressure.
According to the finite element model, reasonable flexion conducts to a stress level close to the limit. Practically, it is very difficult to manipulate the material without breaking it, the test conditions must change very slowly, and the flow topology must be as uniform as possible. Computations shown that the stress produced by the unsteadiness of the conditions has the same order of magnitude than the mechanical one. It was difficult to control everything together in the lab environment, and it will become more complex in the space environment.
The initial idea was to develop a composite material based on Titanium with a thin top surface made of Si-SiC. Unfortunately, these materials have very different thermal properties, and we never succeed in merging them. At high temperature, the thermal stress becomes too high, and the sample either breaks, or the two materials separate at the interface. In the end, it was decided to use only one material and the Si-SiC was selected. The combination of Si-SiC with a more ductile material is still a possible option. Many other approaches are under study. Other materials, ceramic fiber, coating, assembly of smaller elements, active cooling, … are investigated for the future flexible structure under high thermal and mechanical load.

Acknowledgements

The authors gratefully acknowledge the funding under ESA contract no. 4000140022/22/NL/MG (Morphing of Aero-Thermally Loaded Structures).

References

1. Anderson, J. D. (2005). *Introduction to flight.* New York: McGraw-Hill Higher Education. Cleland, J., & Iannetti, F. (1989). *Thermal Protection System of the Space Shuttle.* NASA Contractor Report.
2. Choudhury R., Villace V. F. , Steelant J., Buttsworth D., Marini M. and Di Benedetto S., ' Micro-Aerothermodynamic Analysis of Protuberances on a Hypersonic Glider Using a Reduced Domain Approach', 1st International Conference on High-Speed Vehicle Science and Technology (HiSST), HiSST-2018-1100813, 26-29/11/2018, Moscow, Russia.
3. Buffenoir, F., Pichon, T., & Barreteau, R. (2017). IXV thermal protection system post-flight preliminary analysis. In 7th European Conference for Aeronautics and Space Sciences (EUCASS) (pp. 1-7)
4. Fumo, M., Scigliano, R., Belardo, M., Rufolo, G. C., Esposito, A., & Linari, M. (2015, February). Aero-thermal post flight analysis of IXV control surfaces. In 7Th European

 Copyright © 2025 by author(s)

Conference for Aeronautics and Space Sciences (Eucass), no (pp. 1-11)

5. *Falempin, F. (2008) Ramjet and Dual Mode Operation. In Advances on Propulsion Technology for High-Speed Aircraft (pp. 7-1 – 7-36). Educational Notes RTO-EN-AVT-150, Paper 7. Neuilly-sur-Seine, France: RTO. Available from: http://www.rto.nato.int.*
6. M.BOUCHEZ, V.LEVINE, V. AVRASHKOV, D.DAVIDENKO, P. GENEVIEVE Air breathing space launcher interest of a fully variable propulsion system AIAA – 2000 – 3340 -Huntsville
7. Patrick Gruhn, Ali Gülhan High speed intakes thermal research Educational Notes RTO-EN-AVT-195, Paper 9
8. Steelant J., Varvill R., Defoort S., Hannemann K. and Marini M., 'Achievements Obtained for Sustained Hypersonic Flight within the LAPCAT-II project', 20th Int. Space Planes and Hypersonic Systems and Technology Conference, AIAA-2015-3677, 5-8 July 2015, Glasgow, UK
9. WELLS, W. L. (1985). *Heating measurements on Space Shuttle orbiter models with differentially deflected elevons. Journal of Spacecraft and Rockets, 22(2), 126–133.*
10. Ph. Tran, J.C. Paulat and P. Boukhobza. Re-entry Flight Experiments Lessons Learned – The Atmospheric Reentry Demonstrator ARD. 2007. EUROPEAN AERONAUTIC DEFENCE AND SPACE (EADS ST) LES MUREAUX (FRANCE)
11. David Olynick, Y.-K. Chen and Michael E. Tauber. Aerothermodynamics of the Stardust Sample Return Capsule. JOURNAL OF SPACECRAFT AND ROCKETS. 1999. P 442-462
12. Uyanna, Obinna; Najafi, Hamidreza (2020). Thermal protection systems for space vehicles: A review on technology development, current challenges and future prospects. Acta Astronautica, 176(), 341–356
13. Curry, D. M. (1993). *Space shuttle orbiter thermal protection system design and flight experience* (Vol. 104773). Lyndon B. Johnson Space Center.
14. MOSER, T.; SCHNEIDER, W. (1981). *[American Institute of Aeronautics and Astronautics 1st Flight Test Conference - Las Vegas,NV,U.S.A. (11 November 1981 - 13 November 1981)] 1st Flight Test Conference - Strength integrity of the Space Shuttle Orbiter tiles.*
15. Dotts, R. L., Curry, D. M., & Tillian, D. J. (1985, January). Orbiter thermal protection system. In *Space Shuttle Tech. Conf., Pt. 2*.
16. del Corso, McNeil Cheatwood, Bruce, Hughes, & Calomino, 2011) (Le Coustumer, 1993) (Coiceramics, 2023
17. Dotts, R., Battley, H., Hughes, J., & Neuenschwander, W. (1982). Space Shuttle Orbiter-Reusable surface insulation subsystem thermal performance. *20th Aerospace Sciences Meeting* (p. 5). AIAA
18. Hunt, R. L. (1980). Aerothermal analysis of a wing-elevon cove with variable leakage (No. L-13751).
19. Viladegut, A., Panerai, F., Chazot, O., Pichon, T., Bertrand, P., Verdy, C., & Coddet, C. (2017). Design, integration and preliminary results of the IXV Catalysis experiment. CEAS Space Journal, 9, 141-151.
20. Meyers S., Declercq W., Vleugels J., Van Hooreweder B., Paris S., Debaissieux S., Wouters W., A. Francois A., Parmentier A., E. Kuci and Steelant J., 'Fabrication of reaction bonded silicon carbide components for morphing control surfaces via laser powder bed fusion (LPBF) 3D-printing: challenges and future perspectives', HiSST-2025-241, HiSST 2025, Sept. 22-26, 2025, Tours, France

 Copyright © 2025 by author(s)